A New Integrated Onboard Battery Charger For Electric Scooters

Peng-Hao Huang
Electrical and Computer Engineering
Texas A&M University
College Station, United States
alexamiiah79@tamu.edu

Naresh Rana
Electrical Engineering
Indian Institute of Science
Bengaluru, India
nareshrana@iisc.ac.in

Abhay Gupta
Electrical Engineering
Indian Institute of Science
Bengaluru, India
abhayg.iitk@gmail.com

Prasad Enjeti
Electrical and Computer Engineering
Texas A&M University
College Station, United States
enjeti@tamu.edu

Kaushik Basu
Electrical Engineering
Indian Institute of Science
Bengaluru, India
kbasu@iisc.ac.in

2024 IEEE International Communications Energy Conference (INTELEC) | 979-8-3503-7057-7/24/$31.00 ©2024 IEEE | DOI: 10.1109/INTELEC60315.2024.10678977

***Abstract*—In this paper a new DAB based bidirectional integrated onboard charger for electric scooters is discussed. Utilizing a single-phase matrix converter as a high-frequency AC-AC converter, a high-frequency transformer as isolation, and incorporates semiconductors from the onboard traction inverter as rectifiers to efficiently charge the low-voltage battery. For enhanced safety, high-frequency isolation safeguards the internal traction circuit. Additionally, the onboard electric motor is disengaged during the charging process to protect unintentional power flow. A design example implementing optimal Triple Phase Shift (TPS) modulation with 4-step switching, and minimum RMS current technique is showcased, featuring a 3kW power rating and benchmarking this rating against a conventional off-the-shelf external charger. This approach promises improved integration and convenience in electric scooter charging solutions.**

***Index Terms*—IOBC, EV, LEV, DAB, AC-DC**

I. Introduction

In the rapidly evolving realm of urban mobility, electric scooters and low-power electric vehicles (EVs) are increasingly dominating the market traditionally occupied by light vehicles with internal combustion engines. In rural regions, on the other hand, electric land management machinery, including lawn mowers, agricultural robots, and similar devices for household-scale field operations, are gradually replacing traditional diesel engines. This transition demonstrates an evolving preference towards more sustainable and energy-efficient agricultural practices. These eco-friendly alternatives have become essential in addressing both urban and rural challenges such as air pollution, CO2 emissions, health concerns, and the push for greener transportation options. Furthermore, the escalating demand for lightweight EVs in the Indo-Pacific region underscores the significance of researches focused on the development of lightweight EV technologies.

Traditionally, most EVs require an external charging module or rely on battery swapping at designated exchange stations, a practice that not only complicates usability and diminishes convenience but also imposes additional financial burdens

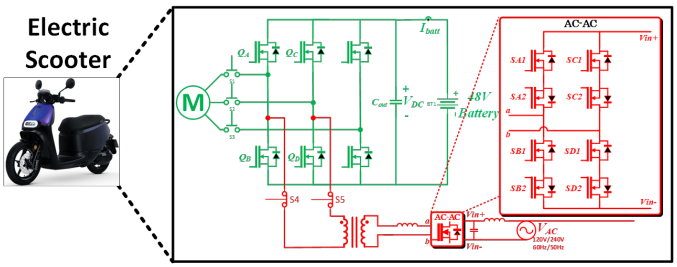

Fig. 1: Proposed integrated on board charger (IOBC) illustration

associated with additional charging module. To address the aforementioned challenges, a crucial element, the integrated onboard battery chargers (IOBCs) is introduced to greatly improve the usability, convenience, and overall cost of lightweight EVs [1]. This vital technology offers users a straightforward plug-and-play charging solution and plays a significant role in enhancing the overall user experience and the operational effectiveness of these vehicles. Additionally, integrating existing electrical components within EVs can reduce the quantity of components required for the charging process, streamlining the overall system architecture.

The major challenges of an IOBC are the considerations of the cost, size, and the weight due to the limited dimensions of an EV [2]. In [3], an IOBC is developed through the augmentation of standard traction inverters with additional AC-DC rectification capabilities, thereby creating a boost Power Factor Correction (PFC) converter. However, this configuration's absence of electrical isolation can potentially lead to accidental damage within the traction circuit. In [4], the author introduces an innovative AC-DC buck-boost circuit designed for LEV charging applications. Despite its novelty, the buck-boost architecture necessitates the inclusion of supplementary DC link capacitors, which could result in increased spatial and weight considerations.

In this study, an additional bi-directional AC-AC converter

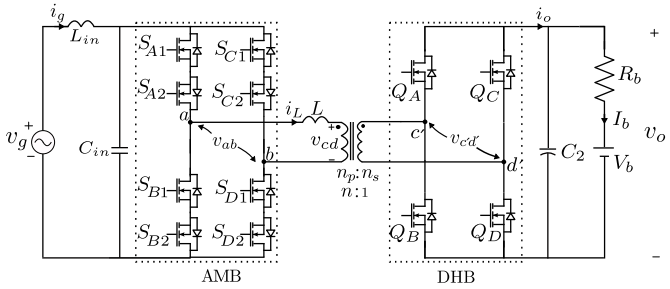

Fig. 2: Proposed Bi-directional AC-DC Converter

integrating with EV's internal 3-phase traction inverter as a rectifier forming an IOBC is introduced. The proposed AC-AC converter incorporates single phase matrix converter to modulate low-frequency AC input into high-frequency AC output and to be rectified by the traction inverter on the secondary side of the high-frequency transformer.

II. Proposed IOBC setup and Analysis

The architecture of the IOBC system is depicted in Fig. 1. The IOBC consists of three primary components: a bi-directional AC-AC converter, high-frequency transformer, and the internal three-phase traction inverter. Within the three-phase traction inverter, two of its legs serve dual functions, operating as a active full bridge rectifier to rectify the high frequency quasi-square wave at the secondary side of the transformer into desired DC level.

Matrix converters, in order to modulate the input to realize the desired output and to accommodate the AC source's intrinsic characteristic by blocking voltage and current in both directions. The converter incorporates four-quadrant bidirectional switches, enhancing its functionality and versatility for AC power conversion.

A. Basic operating principle of proposed IOBC

The circuit representation of the proposed AC-AC converter is illustrated in Fig. 2. This converter is comprised of four bidirectional switches, SA, SB, SC, and SD. Each integrating a pair of Silicon Carbide (SiC) Metal-Oxide-Semiconductor Field-Effect Transistors (MOSFETs) in a common source configuration. These MOSFETs are designed to block voltage and current from both directions with their drain terminals and the cathodes of the body diodes. The converter has two output voltage state that feeds to the series inductor: positive, zero, and negative.

The proposed IOBC, which includes an AC-AC matrix converter, series inductor, and a HFT connected to the full-bridge topology of the traction inverter, forms an AC-DC Dual Active Bridge (DAB) topology. To optimize power transfer from the AC source to the battery, this work employs the modulation technique presented in [5, 6]. Additionally, to achieve unity power factor and maintain power quality when charging the LEV using the full-bridge matrix converter, the triple-phase shift TPS technique with three degrees of freedom is selected for effective implementation.

In the TPS approach, to transfer power from the AC source to the battery, the matrix converter utilizes three voltage states that feed to the inductor: positive, zero, and negative. Equation 1 describes the voltage V_{ab} at the input to the inductor. Equation 2 represents the secondary voltage with respect to the primary side, with $n = \frac{n_p}{n_s}$.

$$V_{ab} = \begin{cases} V_g & SA, SD \text{ on}, SB, SC \text{ off} \\ 0 & SB, SD \text{ off}, SA, SC \text{ on} \\ -V_g & SA, SD \text{ off}, SB, SC \text{ on} \end{cases} \quad (1)$$

$$V_{cd} = \begin{cases} nV_o & QA, QD \text{ on}, QB, QC \text{ off} \\ 0 & QB, QD \text{ on}, QA, QC \text{ off} \\ -nV_o & QB, QC \text{ on}, QA, QD \text{ off} \end{cases} \quad (2)$$

In accordance with the primary voltage states detailed in Eq-1, two control signals, *PWMA* and *PWMB*, are generated by the controller. Both signals have a duty cycle d_1 and are phase-shifted by 180 degrees. *PWMA* serves as the control signal to switch *SA* and *SD* complementarily, while *PWMB* controls *SB* and *SC* in a complementary manner, creating alternating positive, negative, and zero states at the transformer. When *PWMA* is high, indicating the *On* duration for switches *SA* and *SD*, and the *Off* duration for switches *SB* and *SC*, the result is $V_{ab} = V_g$ at the primary side. Conversely, when *PWMB* is high, switches *SA* and *SD* are turned off and switches *SB* and *SC* are turned on, reversing the voltage at V_{ab}. Lastly, when both *PWMA* and *PWMB* are low, switches *SA* and *SC* are off and switches *SB* and *SD* are on, resulting in $V_{ab} = 0$. The durations of the positive and negative states are equal to d_1. Both PWM control signals on the matrix converter side are subsequently processed through a digital 4-step generation circuit, which includes digital delays and logic gates to manage the PWM switching for all SiC MOSFETs. The details of this digital 4-step generation process will be discussed in the following subsection.

Similarly, operating under the TPS method, the full-bridge switches QA, QB, QC, QD switch in the same pattern as the matrix converter to produce $+nV_o$, $-nV_o$, and zero at V_{cd} with a duty cycle d_2. To receive power from the matrix converter, the secondary side voltage pulses V_{cd} should have a phase delay δ relative to V_{ab}. This delay allows the voltage difference between V_{ab} and V_{cd} to charge the inductor current, thereby transferring power. The detailed steady-state analysis is presented in [5], and the control of the duty cycles (d_1, d_2) along with phase shift δ will be further discussed in Section II-D.

B. Proposed Digital Single Phase 4-step Switching

In a conventional unidirectional half-bridge, dead-time is added to prevent short circuits between AC terminals. By utilizing 4-quadrant AC switches, a sequential 4-step switching approach not only prevents short circuits but also ensures continuous inductive current flow eliminating the dead-time effect at the switch node. Correct switching sequences require considering both input voltage polarity and the direction of inductive current. With this in mind, the 4-step commutation

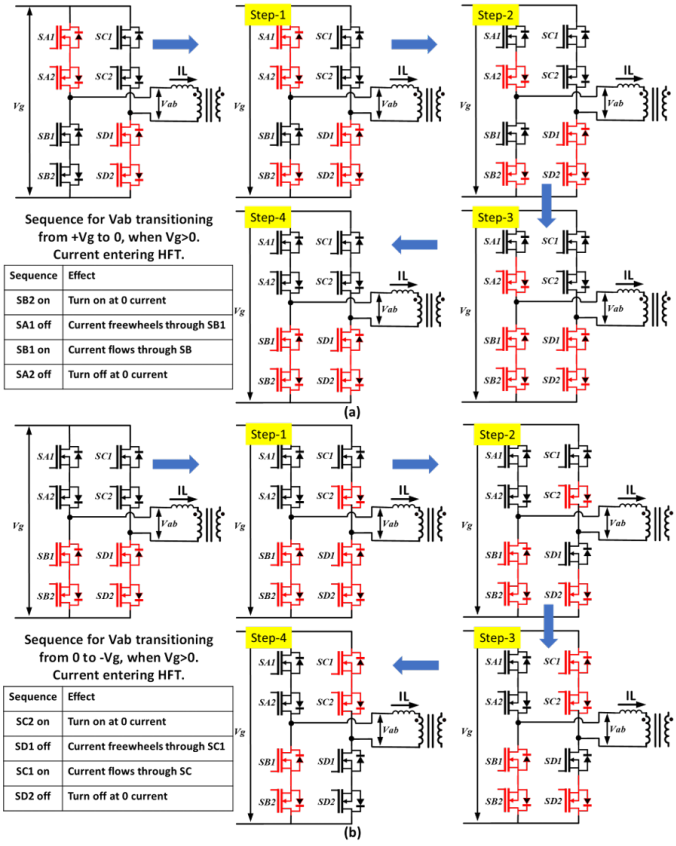

Sequence	Effect
SB2 on	Turn on at 0 current
SA1 off	Current freewheels through SB1
SB1 on	Current flows through SB
SA2 off	Turn off at 0 current

Sequence	Effect
SC2 on	Turn on at 0 current
SD1 off	Current freewheels through SC1
SC1 on	Current flows through SC
SD2 off	Turn off at 0 current

Fig. 3: (a) 4-step switching sequence for V_{ab} transitioning from V_g to 0 when $V_g > 0$ and inductive current entering the transformer. (b) 4-step switching sequence for V_{ab} transitioning from 0 to $-V_g$ when $V_g > 0$ and inductive current entering the transformer.

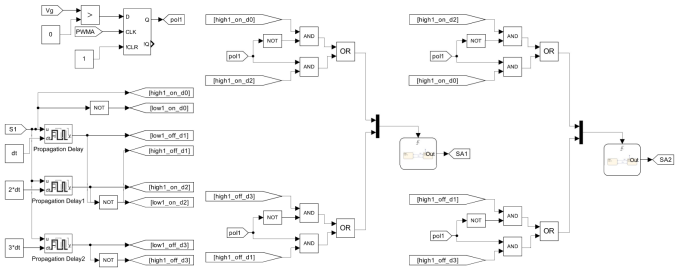

Fig. 4: Proposed digital 4-step switching generator.

$HS\ on \rightarrow LS\ on\ \&\ V_g > 0$	**Action**	**Effects**
Step-1	LS2 on	Turn on at 0 current
Step-2	HS1 off	• $I_L > 0$: LS1 freewheeling • $I_L < 0$: No effect
Step-3	LS1 on	• $I_L > 0$: LS conducting • $I_L < 0$: LS conducting
Step-4	HS2 off	Switching complete
$LS\ on \rightarrow HS\ on\ \&\ V_g > 0$	**Action**	**Effects**
Step-1	HS2 on	Turn on at 0 current
Step-2	LS1 off	• $I_L > 0$: No effect • $I_L < 0$: HS2 freewheeling
Step-3	HS1 on	• $I_L > 0$: HS conducting • $I_L < 0$: HS conducting
Step-4	LS2 off	Switching complete
$HS\ on \rightarrow LS\ on\ \&\ V_g < 0$	**Action**	**Effects**
Step-1	LS1 on	Turn on at 0 current
Step-2	HS2 off	• $I_L > 0$: No effect • $I_L < 0$: LS1 freewheeling
Step-3	LS2 on	• $I_L > 0$: LS conducting • $I_L < 0$: LS conducting
Step-4	HS1 off	Switching complete
$LS\ on \rightarrow HS\ on\ \&\ V_g < 0$	**Action**	**Effects**
Step-1	HS1 on	Turn on at 0 current
Step-2	LS2 off	• $I_L > 0$: HS2 freewheeling • $I_L < 0$: No effect
Step-3	HS2 on	• $I_L > 0$: HS conducting • $I_L < 0$: HS conducting
Step-4	LS1 off	Switching complete

TABLE I: Switching Actions and Effects

should be implemented individually and independently on both legs in the Matrix converter to smooth the transition between high-side and low-side switches, there are overall 4 switching sequences for both legs. Fig. 3 demonstrates this analysis, showing the transition from $V_{ab} = V_g$ to $V_{ab} = 0$, and from $V_{ab} = 0$ to $V_{ab} = -V_g$ in a single-phase matrix converter. All transitions and effects in one leg are generalized in Table-I, with HS and LS representing the switch set connected to $+V_g$ and $-V_g$ respectively.

In Fig. 3(a), at the time when the converter transitions the voltage V_{ab} from V_g to 0, the sequence is as follows: first, turn on $SB2$ at zero current as predecessors to redirect the current. Next, turn off $SA1$ to allow the current to freewheel through $SB1$. Then, turn on $SB1$ to conduct the current through the MOSFET. Finally, turn off $SA2$ at zero current to complete the sequence. In this scenario, turning on $SB1$ first would create a short circuit between two input terminals.

To realize the sequential switching electronically, the aforementioned patterns are implemented using the circuit shown in Fig. 4, illustrating the digital circuit to toggle the $SA1$ and $SA2$. Initially, *PWMA* passes through a delay circuit, generating turn-on and turn-off signals with 0, 1, 2, and 3 unit(s) of delay. These turn-on and turn-off signals are then routed to separate multiplexers (muxes) with the polarity of V_g as the control signal. Finally, the outputs from the muxes are connected to an edge-triggered state machine. When the input turn-on signal transitions from low to high, the state machine outputs high. Conversely, when the input turn-off signal transitions from low to high, it outputs low.

C. Modulation

The AC-DC dual active bridge (DAB) operates like a quasi-static DC-DC DAB because the switching frequency (f_s) is much higher than the line frequency (f_l). The voltage input to the matrix converter, as indicated in Fig. 2, changes slowly over the line cycle.

The AC side Matrix Bridge (AMB) and DC side H-Bridge (DHB) generate a quasi-square waveform. This waveform has half-wave symmetry over the switching cycle T_s. The duty cycle d_1 is the pulse width of v_{ab}, d_2 is the pulse width of v_{cd}, and δ is the phase shift between v_{ab} and v_{cd}.

The analysis is similar to DC-DC DAB [6]. For simplicity,

the system is analyzed in per unit.

$$V_{base} = nV_o, \quad Z_{base} = 2\pi f_s L, \quad I_{base} = \frac{V_{base}}{Z_{base}}, \tag{3}$$

$$S_{base} = V_{base} I_{base} \tag{4}$$

$$\text{Input voltage}, v_g = V_m \sin(\omega t) \tag{5}$$

$$\text{in pu}, m = \frac{V_m \sin(\omega t)}{V_{base}} \tag{6}$$

The equivalent DAB model is shown in Fig. 5. The voltage across nodes a and b, nodes c and d, and the inductor current are illustrated in Fig. 6. The direction of the power flowing between the AC and DC side in Single Phase Shift (SPS) modulation is controlled by δ, as governed by the equation in (7).

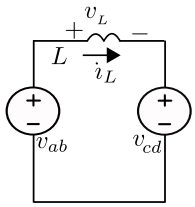

Fig. 5: Equivalent model of DAB

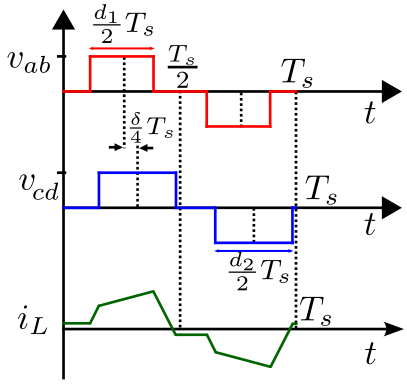

Fig. 6: Voltage at both sides of inductor and current through the inductor in one switching cycle

$$\delta = 1 - \sqrt{1 - \frac{4j}{\pi}} \tag{7}$$

The grid-side current in per unit, denoted as j, which needs to be shaped, is defined by equation (8).

$$j = \frac{I_m \sin(\omega t)}{I_{base}} \tag{8}$$

However, in SPS, the RMS current of the inductor is high, leading to increased conduction loss. This RMS current can be minimized by using triple phase shift modulation (TPS) for a given m and j. The optimal modulation strategy is detailed in TABLES II and III [7].

To optimise for minimal conduction losses on both primary and secondary sides, the transformer turns ratio n and inductance L are determined, given specific power requirements, input and output voltages. The resistances r_s and r_p refer to the primary and secondary sides respectively. The values of n and L can be computed using the methodology outlined in eqn. (13), utilising given parameters such as $V_o, V_m, r_s, r_p, I_o, f_s$[6].

$$M = \frac{7.77K_c - 57.13 + \sqrt{(K_c - 0.17)(248.6 - K_c)}}{3(3.63K_c - 14.89)} \tag{9}$$

$$K_c = \left(\frac{V_o}{V_m}\right)^2 \left(\frac{r_s}{r_p}\right) \tag{10}$$

$$\gamma = -8.461M^5 + 38.66M^4 - 66.04M^3 \tag{11}$$

$$+52.34M^2 - 19.53M + 3.575 \tag{12}$$

$$n = \frac{V_m}{MV_o}, \quad L = \frac{\gamma M V_o}{16 I_o f_s} \tag{13}$$

	j_{c1}	j_{c2}
$m \leq 1$	$\frac{\pi m(1-m)}{2}$	$\frac{(1-m)\pi}{2m^2}(-1 + \frac{1}{\sqrt{1-m^2}})$
$m > 1$	$\frac{\pi(m-1)}{2m^2}$	$\frac{\pi}{2}(1 - m^2 + m\sqrt{m^2-1})$

TABLE II: Current Boundary level

	$j \in [0, j_{c1})$	$j \in [j_{c1}, j_{c2})$	$j \in [j_{c2}, \frac{\pi}{4}]$
$m \leq 1$	$d_1 = \sqrt{\frac{2mj}{(1-m)\pi}}$ $d_1 = md_2$ $\delta = (1-m)d_2$	$\pi d_1(1-\delta) = m\pi(2d_1 - d_1^2) - 2mj$ $d_2 = 1$ $\delta = 1 - \sqrt{2d_1 - d_1^2 - \frac{4j}{\pi}}$	$d_1 = 1$ $d_2 = 1$ $\delta = 1 - \sqrt{1 - \frac{4j}{\pi}}$
$m > 1$	$d_1 = md_2$ $d_2 = \sqrt{\frac{2j}{(m-1)\pi}}$ $\delta = (m-1)d_2$	$d_1 = 1$ $\pi d_2(1-\delta) = \frac{\pi}{m}(2d_1 - d_1^2) - \frac{2j}{m}$ $\delta = 1 - \sqrt{2d_2 - d_2^2 - \frac{4j}{\pi}}$	$d_1 = 1$ $d_2 = 1$ $\delta = 1 - \sqrt{1 - \frac{4j}{\pi}}$

TABLE III: Optimal solution

D. Control

The average switching cycle model of the DAB acts like a current source, as depicted in Fig. 7. Following this, there is a capacitor and a load consisting of a battery and resistance. This forms a first-order system. The transfer function between output voltage (v_o) and DAB output current (i_o) is represented by Eq. 14.

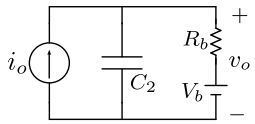

Fig. 7: Switching cycle average model

$$\frac{v_o(s)}{i_o(s)} = \frac{R_b}{1 + sC_2R_b} \tag{14}$$

The block diagram of the voltage controller is depicted in Fig. 8. The output of the voltage controller provides the grid current reference. Based on TABLE III, d_1, d_2, and δ are calculated from the grid current reference.

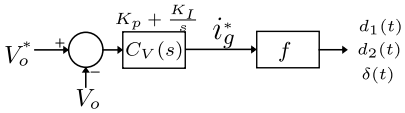

Fig. 8: Block diagram of the control

III. Simulation Results and Discussion

The IOBC is simulated using *Simulink*, with design specifications detailed in Table IV to validate its operation. Fig. 9 shows the input grid-side voltage and current. The THD of the grid current, depicted in Fig. 10, is less than 5%. Due to zero energy stored during each switching cycle, the output current has a second harmonic current, illustrated in Fig. 11; The average current supplied to the battery is 62.5A. Fig. 12 displays the envelopes of v_{ab}, v_{cd}, and i_L, while Fig. 13 shows their waveforms during the switching cycle. Fig. 14 demonstrates v_{ab} transitioning from zero to negative and back to zero triggered by the 4-step switching. Finally, Fig. 15 shows error signal and current reference signal when the controller aims to regulate the battery voltage to 48V, and keeping the sinusoidal current from the source.

Parameter	Value
V_{ac}	240 V
C_{in}	51μF
L_{in}	20μH
L	35μH
C_2	100 μF
Turns Ratio	5.95:1
Charging Current (average)	62.5 A

TABLE IV: Specification

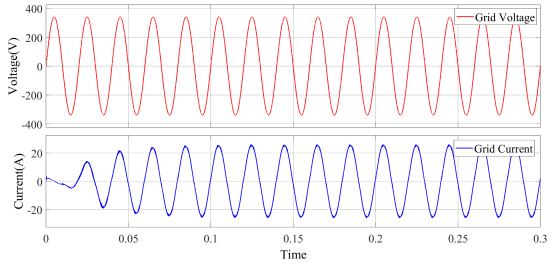

Fig. 9: Input AC voltage and current

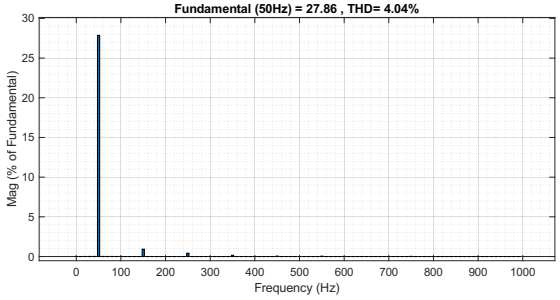

Fig. 10: Harmonics content of grid current

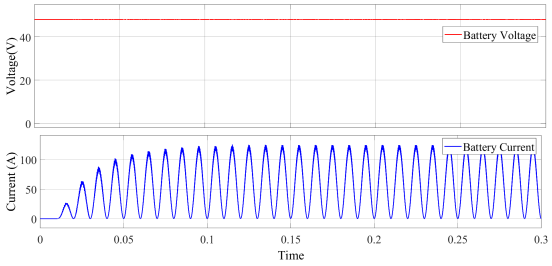

Fig. 11: Output battery voltage and current

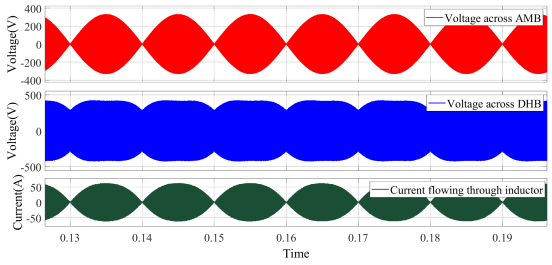

Fig. 12: Volatge from AMB, DHB and current through inductor L

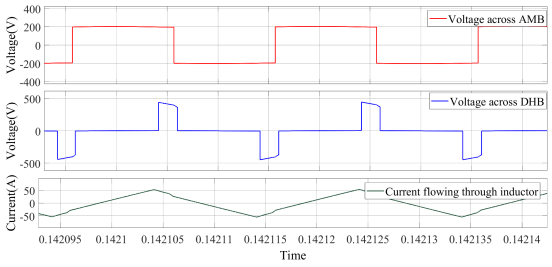

Fig. 13: Volatge from AMB, DHB and current through inductor L in switching cycle

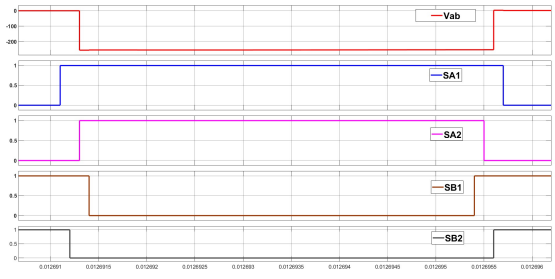

Fig. 14: 4-step sequential switching with v_{ab} voltage transition from zero to negative and negative to zero.

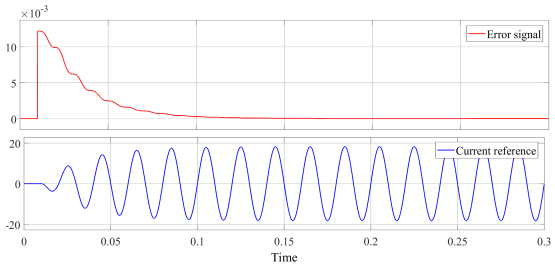

Fig. 15: Signal of controller

IV. Conclusion

A new dual active bridge (DAB) based integrated onboard battery charger (IOBC) for LEVs is demonstrated in this paper. The design of the IOBC incorporates a high-frequency transformer and a bidirectional AC-AC converter, serving as an bridge between wall power and the internal traction inverter, which functions as an AC-DC active rectifier. These critical components ensure electrical isolation of the internal circuit while the AC-DC mechanism eliminates the need for bulky DC-link capacitors. The proposed IOBC was operated using optimal triple phase shift (TPS) modulation with 4-step switching, and minimum RMS current technique. The IOBC design is benchmarked against conventional external E-scooter battery chargers, offering a 3kW charging capacity without an extra H-bridge at DC side, therefore, optimizing the power density. Simulations showed the operation of the proposed IOBC, demonstrating the effectiveness of the solution.

V. Future Work

The hardware realization of the proposed bi-directional AC-DC converter setup will be designed and tested. The control algorithm will be implemented in a digital signal processing (DSP) board and a field programmable gate array (FPGA) module.

References

[1] Mohamed Y. Metwly et al. "A Review of Integrated On-Board EV Battery Chargers: Advanced Topologies, Recent Developments and Optimal Selection of FSCW Slot/Pole Combination". In: *IEEE Access* 8 (2020), pp. 85216–85242. DOI: 10 . 1109 / ACCESS . 2020 . 2992741.

[2] Tuopu Na et al. "A review of on-board integrated electric vehicles charger and a new single-phase integrated charger". In: *CPSS Transactions on Power Electronics and Applications* 4.4 (2019), pp. 288–298.

[3] Gianmario Pellegrino, Eric Armando, and Paolo Guglielmi. "Integrated battery charger for electric scooter". In: *2009 13th European Conference on Power Electronics and Applications*. IEEE. 2009, pp. 1–7.

[4] Aswin Dilip Kumar, Jitendra Gupta, and Bhim Singh. "A Single-Stage Charger for LEV Based on Quadratic Buck-Boost AC-DC Converter Topology". In: *IEEE Transactions on Industry Applications* 59.4 (2023), pp. 4252–4263. DOI: 10.1109/TIA.2023.3259944.

[5] Anping Tong et al. "Modeling and Analysis of a Dual-Active-Bridge-Isolated Bidirectional DC/DC Converter to Minimize RMS Current With Whole Operating Range". In: *IEEE Transactions on Power Electronics* 33.6 (2018), pp. 5302–5316. DOI: 10.1109/TPEL.2017.2692276.

[6] Sayan Paul and Kaushik Basu. "Conduction Loss Minimized Modulation and Design of a DAB-based Single-stage DC to Single-Phase AC Converter for EV Charger Application". In: *IEEE Transactions on Transportation Electrification* (2024), pp. 1–1. DOI: 10.1109/TTE.2024.3395973.

[7] Dibakar Das and Kaushik Basu. "Optimal Design of a Dual-Active-Bridge DC–DC Converter". In: *IEEE Transactions on Industrial Electronics* 68.12 (2021), pp. 12034–12045. DOI: 10.1109/TIE.2020.3044781.